Spring 3-26-2013

Determination of Average Loss Lifetimes for Near-Earth Electrons in Solar Storms

John Blears
Washington University in St Louis

Determination of Average Loss Lifetimes for Near-Earth Electrons in Solar Storms

John Blears
(Dated: February 27, 2013)
Department of Atmospheric Oceanic and Space Science, University of Michigan
Department of Physics, Washington University in St. Louis

The rate of electron wave-particle scattering in the near-Earth magnetosphere is investigated using multiple simulations of solar storms from solar cycle 23 (1996-2005). Simulations are created using the Hot Electron and Ion Drift Integrator (HEIDI) model, which analyzes the drifts of keV-energy electrons through the inner magnetosphere and identifies the precipitation of these particles into the upper atmosphere. The loss lifetime formulation used by HEIDI, which represents the rate at which the keV-energy of the electrons is extinguished, predicts unreasonably large loss lifetimes deep in the inner magnetosphere. This discrepancy between the values used by the HEIDI model and those observed by satellite measurement can in part be resolved as a result of this work, which provides evidence for more reasonable loss lifetimes for particles in the inner magnetosphere. This study and future work can be used to improve data-model comparisons of solar storms.

I. INTRODUCTION

The solar wind is a continuous emission of particles, principally of electrons and protons, by the sun in all directions. The particles are emitted at high speeds, within an approximate range of 400-750 Km/sec, and in large quantities (about 1.3*10^36/sec). This approximates to an average mass loss of one million tons of material per second. [1,2] British astronomer Richard Carrington first proposed the existence of solar wind in 1859, however it wasn't until 1959 that particles were observed directly using hemispherical ion traps aboard Soviet satellite Luna 1. [3]
Since the solar wind contains electrically charged particles, it interacts strongly with the earth's magnetic field. Without the presence of the solar wind, the earth's magnetic field would essentially be a dipole created by the convection of molten metals in the earth's core. However, the presence of the solar wind compresses the magnetic field on the dayside of the Earth, and elongates the magnetic field on the Earth's night side. This phenomenon forms the magnetosphere. Today, numerical modeling makes it possible to simulate the flow of particles from the solar wind, through the magnetosphere and its magnetopause boundary layer, and into the upper atmosphere of the Earth. [4] While on fundamental level it is desirable to understand the mechanisms at work within the solar wind, it is also important to recognize that these phenomena have practical impacts, particularly on disruptions to telecommunications systems. [5]

A. Particle Motion

Charged particles in the solar wind flow around the earth and feel a sunward force when on the earth's night side as shown in Figure 1 below. This force, due to the combined effects of the electric field created by the solar wind and the earth's magnetic field, can pull ions from the solar wind into the magnetosphere. Particles may also enter the magnetosphere from the upper atmosphere of the earth, although particles of this sort account for a much smaller percentage.

Once in the magnetosphere, electric and magnetic fields accelerate particles to energies of keV. Simultaneously, Lorentz forces acting on particles give them helical trajectories around earth's magnetic field lines. As the particles move towards the earth, the magnetic field strength increases, resulting in gradient drift. This gradient drift causes negative particles to flow around the dawn side of the earth and positive ions to travel around the dusk side. Charged particles also feel a co-rotational force from dusk to dawn due to the earth's rotation. This accelerates electrons, which are already flowing in that direction, and slows positive ions moving around the dusk side. If ions are of low enough energy, the co-rotational force will dominate the gradient drift and cause them to move around the dawn side along with the electrons.

The angle between a particle's velocity and the magnetic field it is gyrating around is known as pitch angle. In the non-uniform magnetic field of the earth, pitch angle is dependent on the ratio of a particle's parallel and perpendicular components. Particles traveling along magnetic field lines moving closer to the earth experience an increase in their pitch angle. This is due to the first adiabatic law:

$$\mu = \frac{\frac{1}{2} m v_\perp^2}{B} \qquad (1)$$

which states that a particle's perpendicular energy ($\frac{1}{2} m v_\perp^2$) is proportional to the strength of the magnetic field *(B)* it is in. As the particle nears earth, both the magnetic field strength and the perpendicular component of the particle's velocity increase. Due to conservation of energy, as the particle's perpendicular velocity increases, its parallel component decreases, eventually reducing to zero. This point corresponds to a pitch angle of ninety degrees and is referred to as a mirror point.

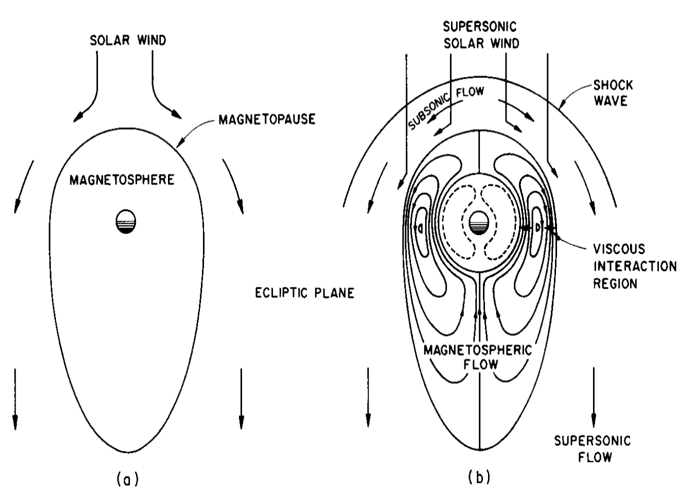

FIG. 1. Flow of ions into magnetosphere [6]

When a particle reaches a mirror point, it begins traveling along the magnetic field line in the reverse direction until it arrives at another mirror point. This motion from mirror point to mirror point traps the particle in "bounce motion" and is illustrated in Figure 2. If the mirror point occurs inside the earth's atmosphere, it will likely be lost to the processes of heating and ionization, as can be observed by the aurora. Loss of this nature is termed pitch angle scattering. The occurrence of pitch angle scattering can be predicted by identifying those particles whose equatorial pitch angle falls inside a solid angle, called the loss cone, centered on the magnetic field line. A theoretical loss cone is portrayed below in Figure 3. The size of a particle's loss cone is dependent on the strength of the magnetic field and therefore on its radial distance from the earth. Particles at larger radial distances feel weaker magnetic fields and have smaller loss cones. If a particle's pitch angle is known to be inside the loss cone, it is safe to predict that it will be lost within a couple of bounce cycles. A particle traveling outside of its loss cone will remain in bounce motion unless various physical processes, such as electromagnetic hiss and chorus waves, scatter the particle into its loss cone. Particles that never enter their loss cones eventually drift to the dayside of the earth and are reintroduced into the solar wind.

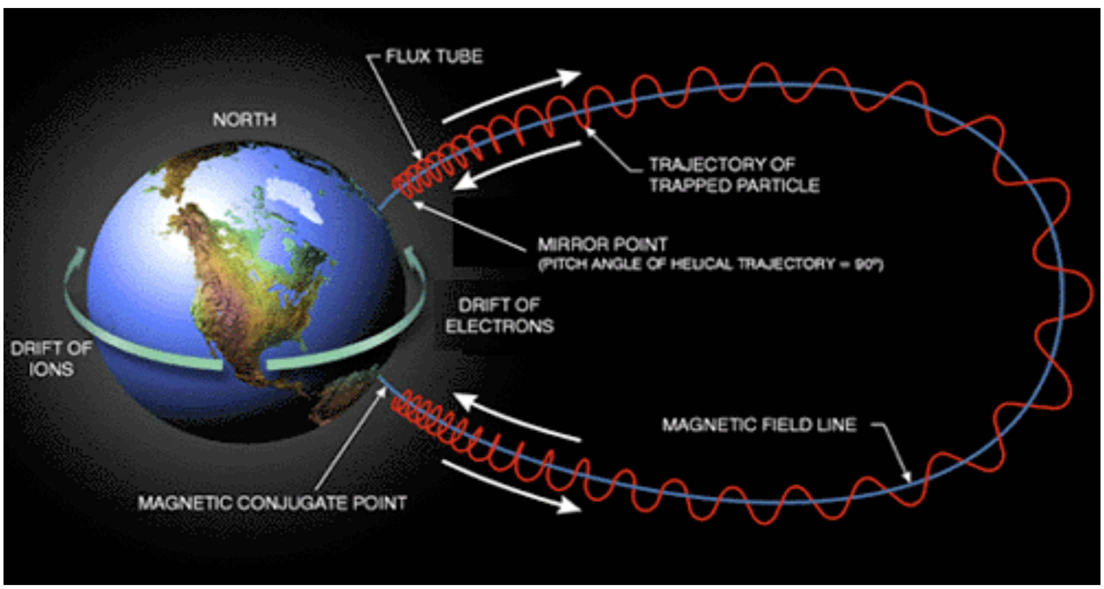

FIG. 2. Particle drift and "bounce motion" [7]

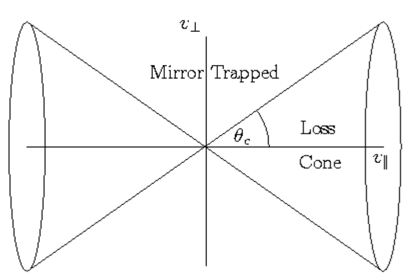

FIG 3. Particle loss cone [8]

B. Solar Storms

Certain events cause large increases in the number of charged particles in the solar wind. These events, called solar storms, are associated with intensified electric fields and have multiple drivers. Two such drivers for solar storms are coronal mass ejections (CMEs) and corotating interaction regions (CIRs). CMEs are a product of the phenomenon of magnetic reconnection occurring near the sun's surface. CIRs on the other hand, originate when fast streams of space plasma overtake slower ones and increase their energy. When a solar storm of either type occurs, particles enter the earth's magnetosphere in a rapid main phase and then slowly precipitate or exit on the dayside during a recovery phase. Solar storms can adversely affect satellite electronics, power grids, and other electronic systems, so understanding the magnetosphere's interactions with them is important.

C. Storm Simulation

There are several numerical models capable of simulating the dynamics of energetic particles in the magnetosphere during solar storms. The model used in this study is the hot electron and ion drift integrator (HEIDI) inner magnetospheric drift physics model, developed in the 1990s at the University of Michigan by *Fok et al.* (1993) [9], *Jordanova et al*. (1996) [10], and *Liemohn et al.* (1999). HEIDI utilizes the Chen and Schulz formulation to estimate loss lifetimes for near-earth particles during solar storms. [11] The formulation combines two scattering rates: "strong" outside and "less than strong" inside. The resultant loss lifetime prediction has a high spatial dependence and is shown in Figure 4. The minimum loss lifetime according to the formulation is about an hour and a half and occurs slightly above six earth radii. Loss lifetimes steadily rise from the minimum to about a week at twelve earth radii.

The limitation of the Chen and Schulz formulation is that it over predicts loss lifetimes deep in the inner magnetosphere. This formulation estimates loss lifetime values greater than a year below five earth radii. On the time scale of a solar storm, which typically last between one and two days, these loss lifetimes are effectively

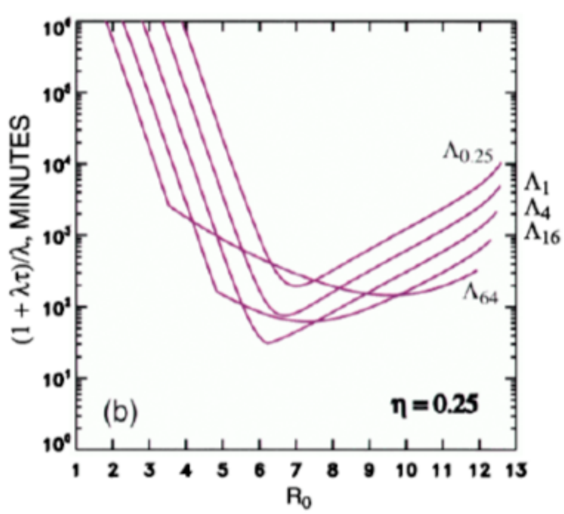

FIG. 4. Chen and Schulz formulation [11]

infinite. This distorts model results for a storm's recovery phase because the total energy content is kept elevated by the contribution of particles that should have undergone pitch angle scattering but are retained as model components. An adjustment to recognize this is made by incorporation of an average maximum loss lifetime, τ_{max}, into the HEIDI model for this study. Running HEIDI with many τ_{max} values (No C-S, infinite, 3 hours, 4 hours, 6 hours, 8 hours, 12 hours, 24 hours, 36 hours, and 48 hours) allows for identification of a value that can best model particle dynamics of storms from solar cycle 23 (1996-2005). The τ_{max} equal to "No C-S" indicates the Chen and Schulz formulation is not applied to HEIDI.

II. METHODS AND PROCEDURE

The HEIDI model averages gyration and bounce motion and solves the kinetic equation for the phase space density of hot plasma species in the inner magnetosphere (e^-, H^+, He^+, and O^+). The equation HEIDI solves for the phase-space density $f(t, R, \varphi, E, \mu_0)$ of one or more ring current species is as follows:

$$\frac{\partial f^*}{\partial t} + \frac{\partial}{\partial \overrightarrow{R_\perp}}\left\{\left\langle \frac{d\overrightarrow{R_\perp}}{dt\overrightarrow{E}}\right\rangle f^*\right\} + \frac{\partial}{\partial E}\left\{\left\langle \frac{dE}{dt\overrightarrow{E}}\right\rangle f^*\right\}$$
$$+\frac{\partial}{\partial \mu_0}\left\{\left\langle \frac{d\mu_0}{dt\overrightarrow{E}}\right\rangle f^*\right\} = \frac{\partial}{\partial E}\left\{\left\langle \frac{dE}{dtCC}\right\rangle f^*\right\} \qquad (2)\ [12]$$
$$+\frac{\partial}{\partial \mu_0}\left\{\left\langle D_{CC}\right\rangle \frac{df^*}{\partial \mu_0}\right\} - \frac{f^*}{\tau_{CE}} - \frac{H(\mu_0-\mu_{0LC})f^*}{0.5\tau_b}$$

Where f is related to f^* by the variable-dependent multiplier in the equation below:

$$f = \frac{f^*}{R_0^2\mu_0 h(\mu_0)\sqrt{E}} \qquad (3)\ [12]$$

The independent variables for phase space density are, in order, time, geocentric distance in the equatorial plane (in units of R_E), magnetic local time (φ = 0 at midnight, increasing eastward), kinetic energy (in keV), and cosine of equatorial pitch angle. HEIDI factors in convective and magnetic drift (left hand side of Eq. *(2)*), Coulomb collision scattering and energy decay (first two terms on the right side of Eq. *(2)*), charge exchange (third term on the right side of Eq. *(2)*), and atmospheric precipitation (last term on the right side of Eq. *(2)*). [11] Night side outer boundary data for HEIDI is attained from magnetospheric plasma analyzer (MPA) instruments and synchronous orbiting particle analyzer (SOPA) instruments onboard the geosynchronous satellites operated by Los Alamos National Laboratory (LANL). [13,14,15]

Output data from HEIDI can be used in conjunction with interactive data language (IDL) to create a series of plots that aid in understanding a storm's particle dynamics qualitatively and quantitatively. Quantitative plots are compared with data from LANL satellites near the earth's noon to check for accuracy. The noon position for satellites is desired because it is the farthest point on the drift path of electrons traveling in the inner magnetosphere from the night side boundary. When analyzing data from a given solar storm, qualitative plots are first generated to get general information such as storm strength, storm duration, and satellite location. Using the information from qualitative plots then aids in the creation of quantitative plots for numerical analysis.

A. Qualitative Plots

Perturbation of the Earth's magnetic field due to a solar storm can be measured by averaging readings from ground-based magnometers located strategically across the globe. As storm intensity increases, the values of these readings (termed Dst*) decreases. Plotting observed Dst* provides an idea of the overall timing and strength of a solar storm. An example of a characteristic Dst* plot is shown below in Figure 5. Typically, a storm's main phase can be identified by locating where the Dst* value transitions to a minimum. After this minimum value (maximum storm intensity), storms enter a recovery phase usually identifiable by the Dst* value slowly returning to baseline. Modeled Dst* traces incorporate the different values for τ_{max} and the plot displays their RMS errors with respect to observed measurements. Note in Figure 5 that for the Dst* model values of τ_{max} for "No C-S" and infinity, the storm intensity is over predicted, as was anticipated. This can be seen by the purple and blue model traces that are overly negative relative to observation. The τ_{max} of infinity corresponds to the unmodified application of the Chen and Schulz formulation.

An idea of how charged particles flow around the earth can be obtained from pressure plots. These plots show either individual ring current species or combinations of them for various values of τ_{max} in half hour increments. Figures 6 and 7 on the following page depict respectively the flow of electrons around earth's dawn side and positive ions around the dusk side. Note that both species enter the magnetosphere from the night side of earth. In comparison to Figures 8 and 9 on page 8, the model shows that high τ_{max} values do not permit ring current particles to properly scatter over time. Lower values of τ_{max} however, allow particles to leave the ring current and improve model results for the recovery phase

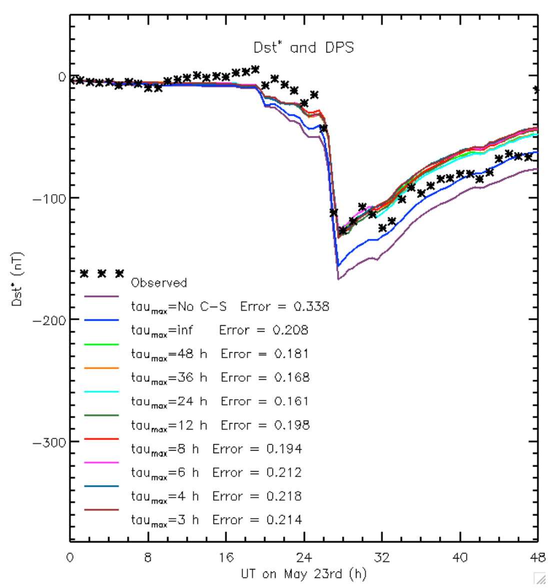

FIG. 5. Dst* plot (May 23rd-24th, 2000)

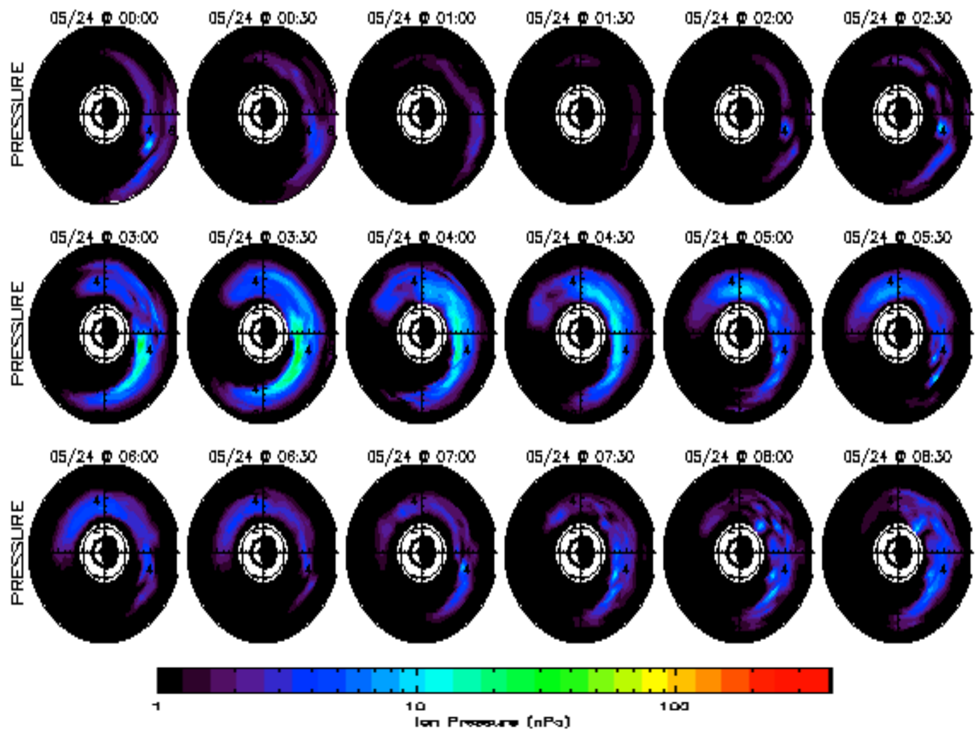

FIG. 6. Electron pressures with τ_{max} of three hours (May 24th, 2000)

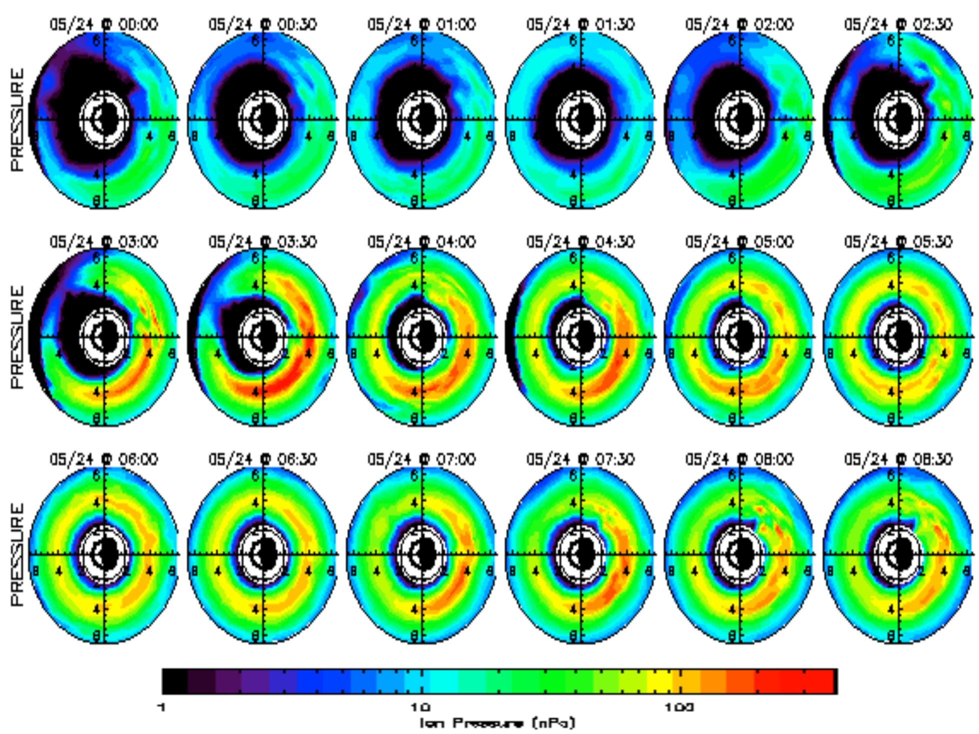

FIG. 7. Combined H^+ and O^+ pressures with τ_{max} of three hours (May 24th, 2000)

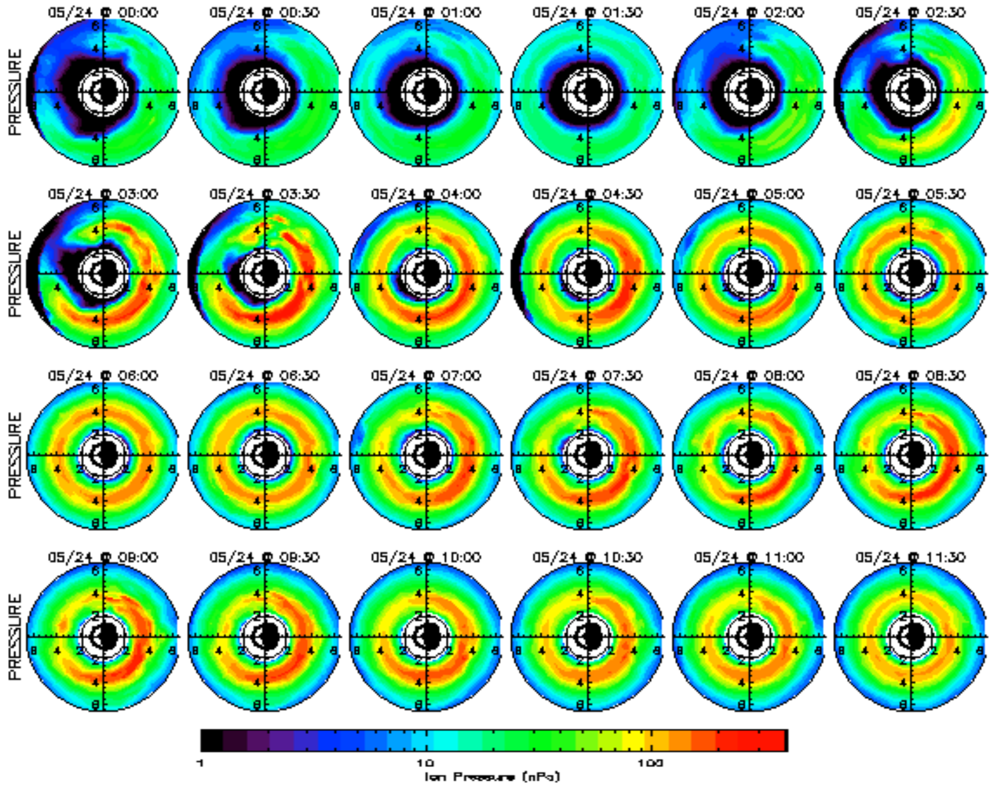

FIG. 8. Pressures for all species with infinite τ_{max} (May 24th, 2000)

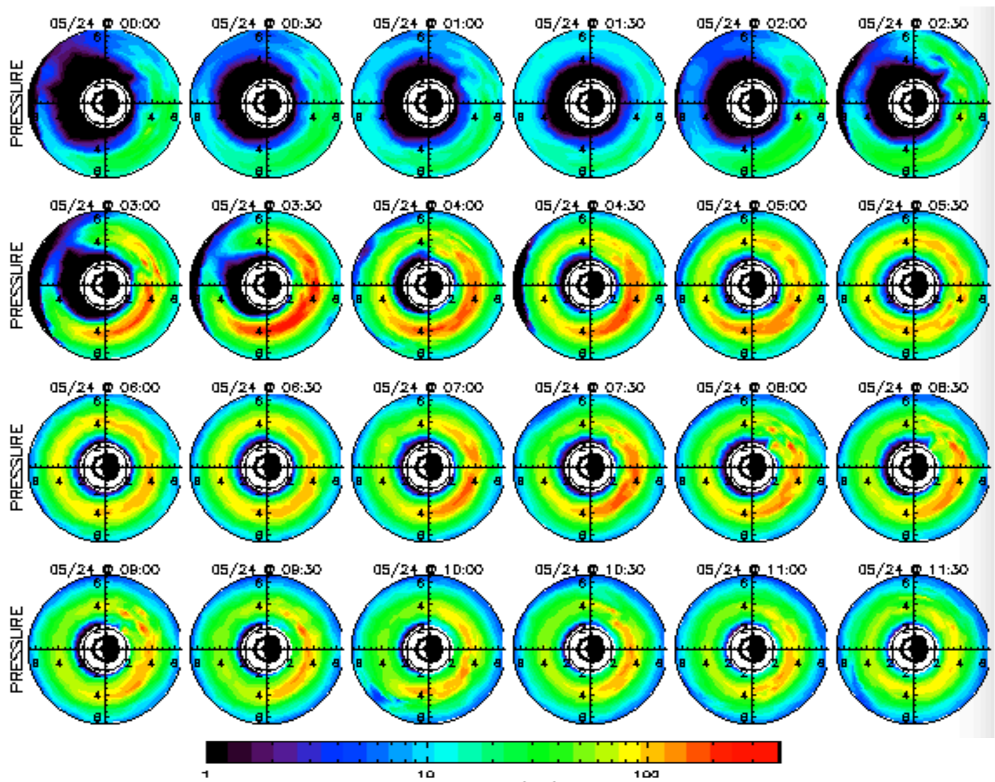

FIG 9. Pressures for all species with τ_{max} of three hours (May 24th, 2000)

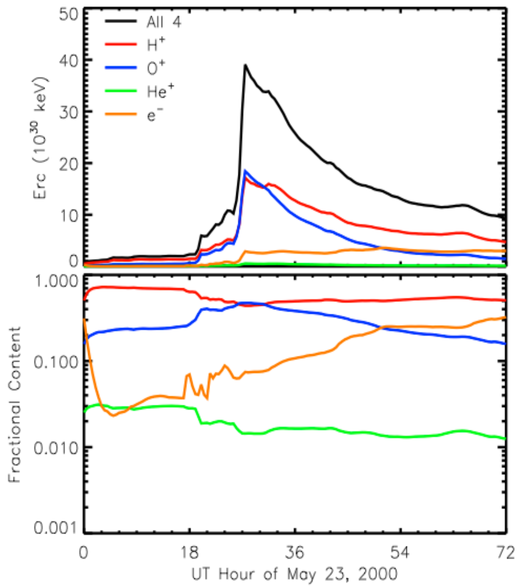

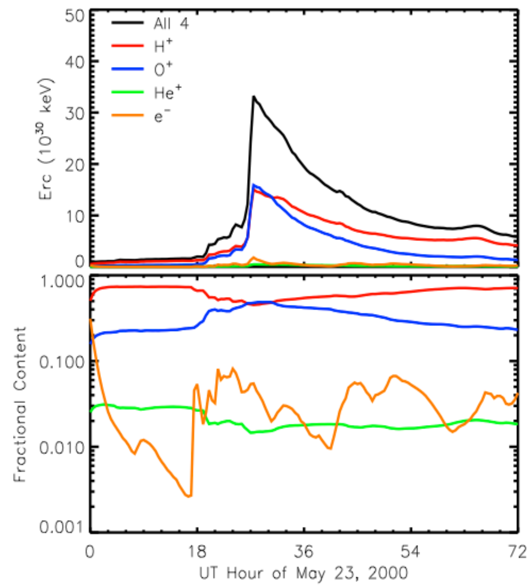

FIG. 10. (Left) Energy fractions with infinite τ_{max} (May 23rd-25th, 2000)
FIG 11. (Right) Energy fractions with τ_{max} of three hours (May 23rd-25th, 2000)

Evidence from plots depicting the fractional contribution made by each particle species to the total energy also supports a faster scattering rate for electrons in the inner magnetosphere. These plots show all four species' energy contribution and their sum together, and so only one energy fraction plot is needed for each value of τ_{max}. Plots for τ_{max} values of infinity and three hours are displayed above in Figure 10 and Figure 11. It is known from previous work that electron energy fraction usually does not exceed ten percent of total energy during the recovery phase. Therefore, these plots also support the idea that a lower τ_{max} is needed in order to more accurately model the precipitation of electrons.

The final qualitative plot used in this project visually displays electron flux energy as measured by LANL geosynchronous satellites and corresponding HEIDI results. Satellite positions relative to Greenwich meridian time are indicated on this plot via the white and black vertical dotted lines is shown in Figures 12 and 13. These lines respectively represent local noon and local midnight times for the satellite. The top panel of each plot displays the energy flux of electrons as observed by LANL MPA instruments, while the bottom panel shows HEIDI model results. In Figure 12 HEIDI model results have an infinite τ_{max} and are too high in energy flux throughout the storm in comparison to LANL data. Figure 13, with a τ_{max} of twelve hours, has reduced electron flux energy that matches LANL MPA data more closely.

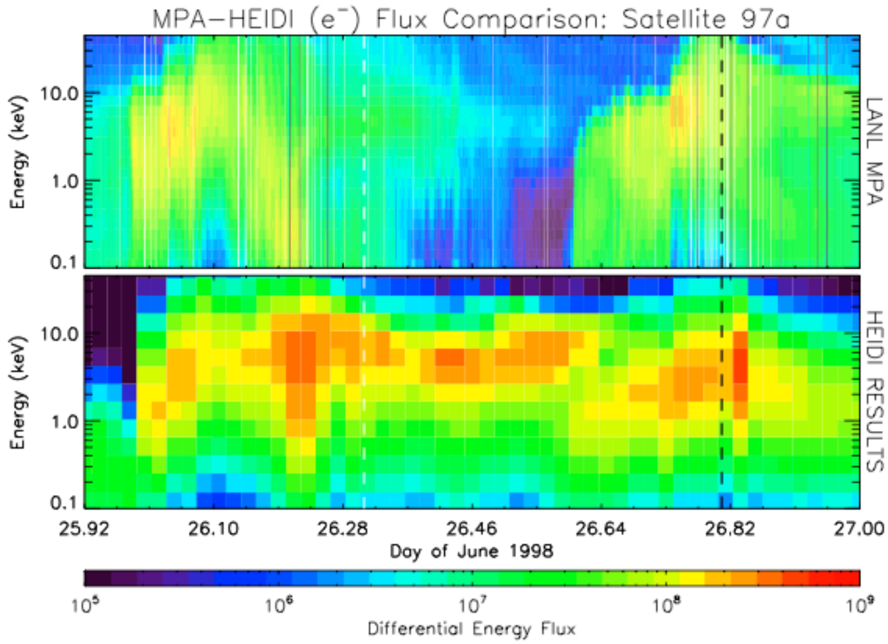

FIG 12. Electron energy flux comparison of LANL satellite 97a with infinite τ_{max}

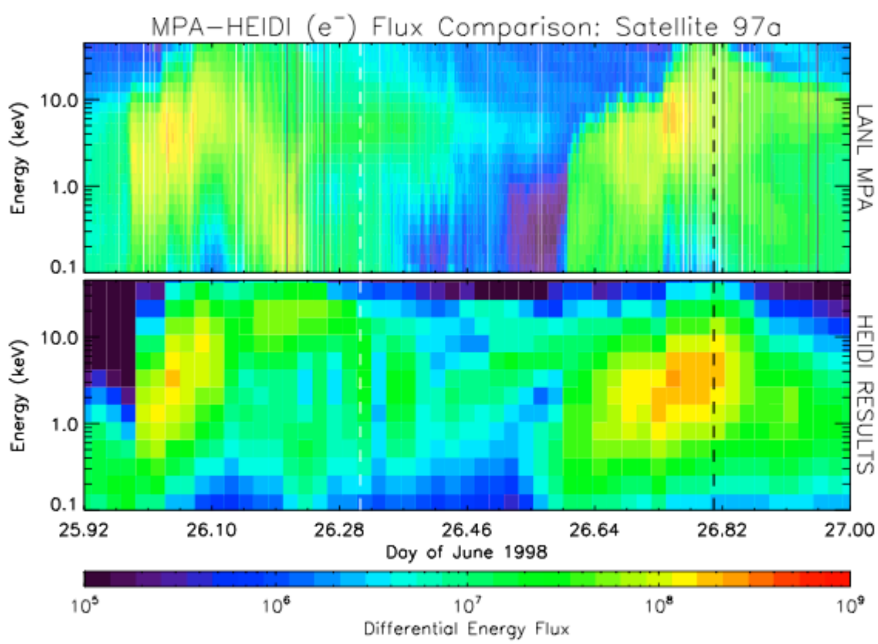

FIG 13. Electron energy flux comparison of LANL satellite 97a with τ_{max} of twelve hours

B. Quantitative Plots

To objectively find a τ_{max} value that optimizes accuracy of data-model comparisons, quantitative plots are needed. While some quantitative data is gained from the Dst* plot, much more data can be obtained by comparing the HEIDI model to MPA values at multiple specified energies in a "flux time error" plot. By computing error in this way, more data points for each τ_{max} can be generated. The resulting data-model comparison at energies of .2 keV, .5 keV, 1.5 keV, and 3.0 keV for LANL satellite 97a during the storm that occurred June 26th 1998 is shown below in Figure 14. This is the same storm plotted in Figures 12 and 13. Note that the IDL code looks at data one hour before and three hours after the local noon of the satellite. Again, this is because the noon position is the farthest point on the drift path of electrons traveling in the inner magnetosphere. It is possible to compare the HEIDI model to MPA values at specific times across the energy range via a "flux energy error" plot, but the IDL code for computing such errors is unfortunately erroneous and the plots are therefore only qualitatively helpful.

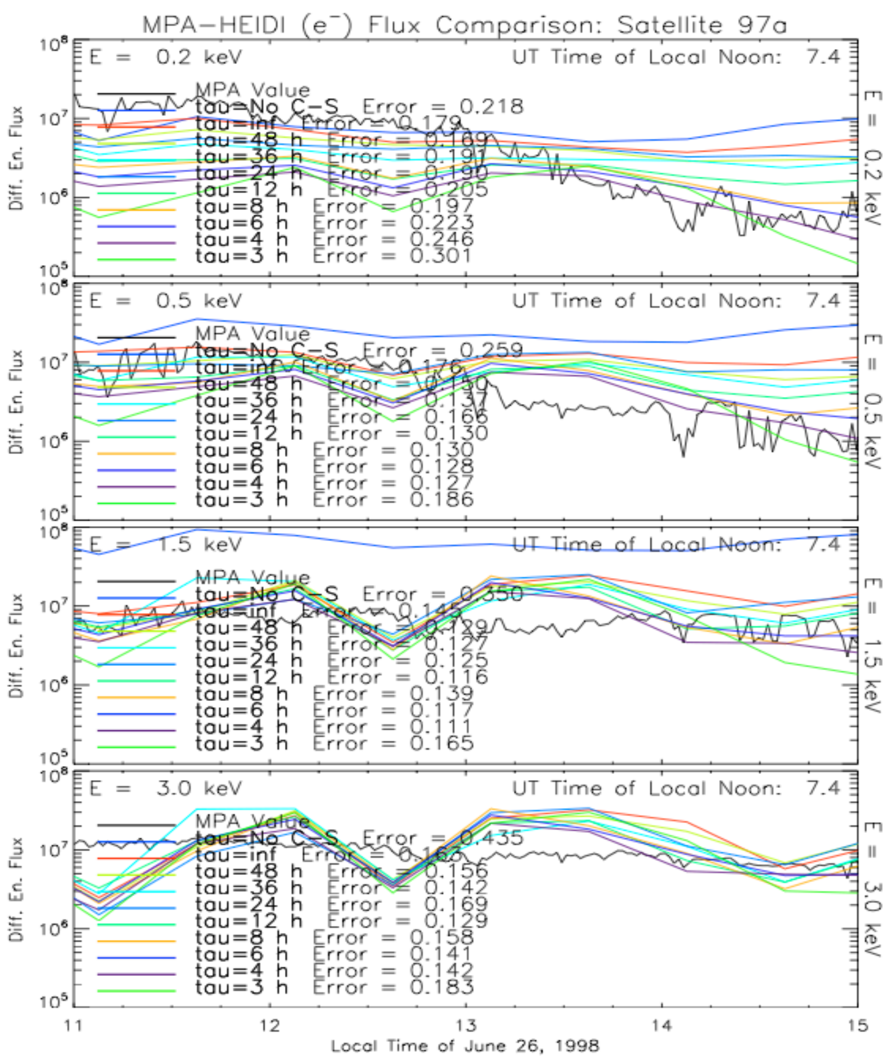

FIG. 14. Flux time error for LANL satellite 97a (June 26th, 1998)

III. RESULTS

To arrive at the optimal value for τ_{max}, the series of plots outlined in section II were created for as many solar storms as was possible over the duration of this study. Ultimately, results were complied from twenty-nine satellite readings during seventeen storms and used to calculate a single overall average error value for each τ_{max}. Overall τ_{max} error averages were computed using a simple mean calculation, averaging values from all valid Dst* and flux time error plots. Some satellite data was unusable either due to lack of LANL data or because the satellite had been traveling outside the magnetosphere, in the solar wind. Overall error averages are summarized in Table 1. Error averages were also calculated for the specific energies of the flux time error plots as is displayed in Table 2. Finally, by identifying the satellites local noon relative to the time of Dst* minimum, average errors were calculated for the main and recovery phases as shown in Table 3 on the following page.

Overall Error	(29 Satellites)	
Tau_max	Error Total	Error Average
No C-S	63.295	0.476
inf	49.183	0.370
48 h	46.892	0.353
36 h	45.934	0.345
24 h	45.006	0.338
12 h	42.647	0.321
8 h	38.75	0.323
6 h	41.041	0.321
4 h	43.222	0.325
3 h	45.081	0.339

Table 1. Overall average errors for various τ_{max} values

Error (0.2 KeV)	(29 Satellites)		Error (0.5 KeV)	(29 Satellites)	
Tau_max	Error Total	Error Average	Tau_max	Error Total	Error Average
No C-S	9.082	0.313	No C-S	13.013	0.449
inf	8.827	0.304	inf	10.905	0.376
48 h	8.488	0.293	48 h	10.413	0.359
36 h	8.119	0.280	36 h	10.080	0.348
24 h	8.234	0.284	24 h	9.925	0.342
12 h	7.819	0.270	12 h	9.230	0.318
8 h	7.094	0.273	8 h	7.779	0.299
6 h	7.750	0.277	**6 h**	8.212	0.293
4 h	9.199	0.317	4 h	8.598	0.296
3 h	10.376	0.358	3 h	8.897	0.307
Error (1.5 KeV)	(29 Satellites)		Error (3.0 KeV)	(29 Satellites)	
Tau_max	Error Total	Error Average	Tau_max	Error Total	Error Average
No C-S	16.370	0.564	No C-S	16.678	0.575
inf	11.310	0.390	inf	11.374	0.392
48 h	10.521	0.363	48 h	10.653	0.367
36 h	10.329	0.356	36 h	10.738	0.370
24 h	9.933	0.343	24 h	10.401	0.359
12 h	9.278	0.320	**12 h**	9.628	0.332
8 h	8.416	0.324	8 h	9.308	0.358
6 h	8.696	0.311	6 h	9.725	0.347
4 h	8.731	0.301	4 h	9.708	0.335
3 h	9.009	0.311	3 h	9.746	0.336

Table 2. Energy specific average errors for various τ_{max} values

Main Phase	(8 Satellites)		Recovery Phase	(21 Satellites)	
Tau_max	**Error Total**	**Error Average**	**Tau_max**	**Error Total**	**Error Average**
No C-S	18.178	0.568	No C-S	36.965	0.440
inf	15.508	0.485	inf	26.908	0.320
48 h	14.513	0.454	48 h	25.562	0.304
36 h	14.281	0.446	36 h	24.985	0.297
24 h	13.910	0.435	24 h	24.583	0.293
12 h	12.564	0.393	12 h	23.391	0.278
8 h	11.189	0.400	8 h	21.408	0.282
6 h	13.702	0.428	**6 h**	20.681	0.259
4 h	13.928	0.435	4 h	22.308	0.266
3 h	15.467	0.483	3 h	22.561	0.269

Table 3: Main and recovery phase average errors for various τ_{max} values

Table 1 suggests that there is no specific τ_{max} that provides a single best scattering rate. Instead, it appears that a range of values produces equally accurate data-model comparisons. Tables 2 and 3 imply a possible explanation for this unexpected finding: τ_{max} could be a variable function dependent on particle energy and storm phase. Possible physical explanations for this will be discussed later. To investigate if τ_{max} is indeed a function of energy the lowest average error values of τ_{max} from Table 2 were plotted against energy. After fitting the data with linear, polynomial, exponential, and power fits, it was determined that a power fit provided the most accuracy. The log-log plot of the power fit is shown in Figure 15. Error bounds for the energy dependent function at each energy were based on the minimum and maximum values of τ_{max} given by the different fits. Error bounds were determined in this manner because each point on the graph represents the τ_{max} value chosen at the given energy that had the lowest average error from data from 29 satellites; thus making it difficult to assign specific error values for τ_{max} at each energy. The minimum error value of τ_{max} of twelve hours for 3 keV was assumed to be an outlier and a τ_{max} value of three hours was used in the making of this plot (which had a very similar error average). The data appears to level off rapidly at higher energies so it is unlikely that this assumption would have a profound effect either way.

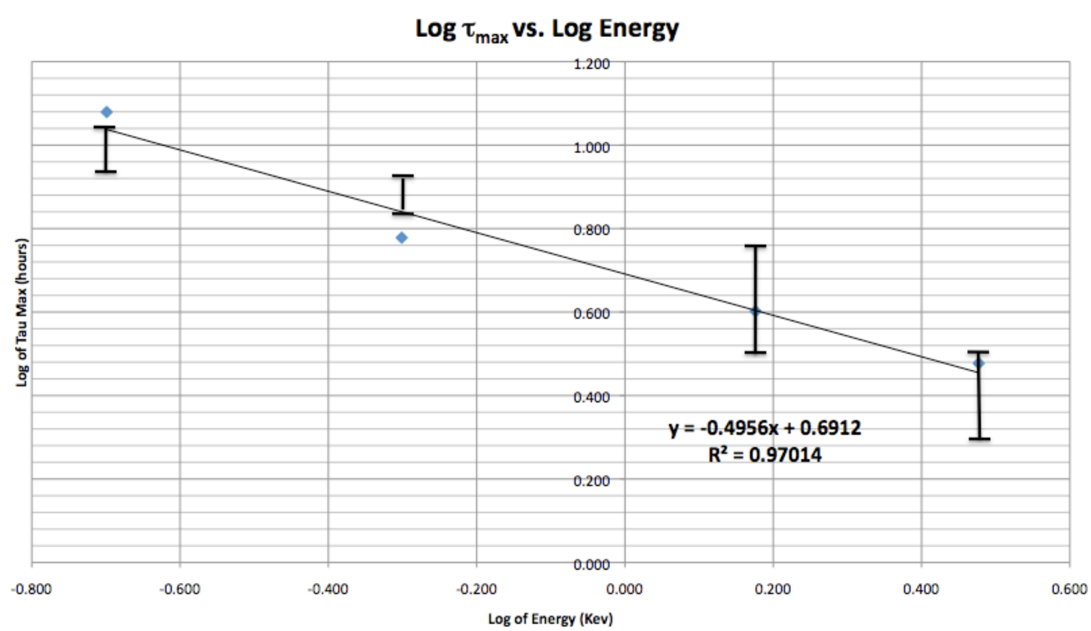

FIG. 15. Energy dependent log τ_{max} vs. log energy function

IV. DISCUSSION

Table 1 indicates that a τ_{max} between six and twelve hours represents the most accurate value that can be applied to HEIDI data-model comparisons. This supports the original hypothesis that loss lifetimes estimated by the Chen and Schulz formulation for near-earth electrons are overestimated. The optimal τ_{max} values are lower than those of over a year given by Chen and Schulz. These lower τ_{max} values have improved accuracy compared to the previous effectively infinite values. Although a range of τ_{max} values stand out as superior alternatives to the old formulation, Table 2 provides initial evidence that τ_{max} may be energy dependent. This evidence is further supported by Figure 15, which shows that an energy dependent power fit yields a strong R^2 correlation. A physical explanation for this energy dependent scattering could be the presence of chorus waves, which scatter higher energy particles more efficiently. Another interesting trend in the data arises from Table 3, which shows that a higher τ_{max} better models a storm's main phase than its recovery phase. This result could be due to intermittent injections of higher energy particles during the recovery phase that may be scattered more rapidly by chorus waves. Preliminary work has been undertaken to modify the HEIDI code to incorporate the energy dependent power function for τ_{max} found in this study. The energy dependent function however, can produce unrealistic τ_{max} values for very high or low energy particles. In light of this, the value of τ_{max} for particles of energy lower than .2 keV or greater than 3 keV will be fixed in the HEIDI code. For particles below .2 keV, the fixed value will be the τ_{max} value given by the power fit at .2 keV. For particles above 3 keV, the fixed τ_{max} value will be the τ_{max} value given by the fit at 3 keV.

Future work may be undertaken to verify that the energy dependent version of HEIDI actually improves data-model accuracy. This could be accomplished by running the energy dependent HEIDI code on storm data already analyzed and comparing the accuracy of results to those given by the old version. It would also be useful to compare results with those from a version of HEIDI, which uses only one τ_{max} value selected from within the optimal range. Additionally, future work could also incorporate a function of τ_{max} dependent on storm phase derived from the data in Table 3.

As well as investigating these apparent trends further, efforts could also be made to improve the predictive robustness of this project. For example, more data could be generated by analyzing more storms. Data volume could also be essentially doubled if the IDL code for computing errors on the flux energy error plots was fixed and run on past storms. Furthermore, this would help determine whether or not τ_{max} is time dependent. If applying an energy, phase, or time dependent function to τ_{max} does improve data-model accuracy, efforts could be made to determine if τ_{max} is dependent on other factors, such as the storm drivers previously referenced. Although it would require substantial time and effort HEIDI could also be adapted to incorporate loss lifetime formulations other than the Chen and Schulz formulation, such as that of Sphrits [16]. Another improvement in result accuracy and timeliness could be attained if the process of calculating errors was automated to remove human error. While this is not an exhaustive list of improvements, much could be learned through their implementation.

A. Acknowledgements

I would like to thank Dr. Liemohn for supervising this work and the University of Michigan AOSS department for their additional assistance during the summer of 2012. Their knowledge and financial support has made this project possible. Results of this project have been incorporated into a paper submitted for publication in the American Geophysical Union. [17] I would also like to acknowledge and thank Dr. Israel for his guidance as well as the Washington University in St. Louis Physics department. I appreciate the opportunity given to me to work on this project and thank all others who helped me in the process.

References:

[1] Feldman, U.; Landi, E.; Schwadron, N. A. (2005). "On the sources of fast and slow solar wind". *Journal of Geophysical Research* 110 (A7): A07109.1–A07109.12.
[2] Kallenrode, May-Britt (2004). *Space Physics: An Introduction to Plasmas and*. Springer.
[3] Harvey, Brian. *Russian planetary exploration: history, development, legacy, prospects*. Springer, 2007, p.26. ISBN 0-387-46343-7.
[4] Encrenaz, Thérèse; Bibring, J.-P.; Blanc, M. (2003). *The Solar System*. Springer.
[5] AT&T Release Re. Telstar 401, 1/11/97.http://www.istp.gsfc.nasa.gov/istp/cloud_jan97/att.html
[6] Liemohn, M. Near Earth Electrons (and Ions). REU Intro Presentation, May 2012. AOSS Department, University of Michigan.
[7] Jursa, A. S. Figure 5-10 in the "Handbook of Geophysics and the Space Environment". United States Air Force, 1985. http://pluto.space.swri.edu/image/glossary/pitch.html.
[8] Hutchinson, I.H. Introduction to Plasma Physics, Chaper 2 "Motion of Charged Particles in fields", 2001. http://silas.psfc.mit.edu/introplasma/chap2.html.
[9] Fok, M.-C., J. U. Kozyra, A. F. Nagy, C. E. Rasmussen, and G. V. Khazanov (1993), A decay model of equatorial ring current and the associated aeronomical consequences, J. Geophys. Res., 98, 19,381, doi:10.1029/93JA01848.
[10] Jordanova, V. K., L. M. Kistler, J. U. Kozyra, G. V. Khazanov, and A. F. Nagy (1996), Collisional losses of ring current ions, J. Geophys. Res., 101, 111, doi:10.1029/95JA02000.
[11] Chen, M. W., and Schulz M. (2001), Simulations of Diffuse Aurora with Plasma Sheet Electrons in Pitch Angle Diffustion Less than Everywhere Strong. Journal of Geophysical Research, Vol. 106, No. A12, Pages 28949-28966.
[12] Liemohn, M. W., A. J. Ridley, J. U. Kozyra, D. L. Gallagher, M. F. Thomsen, M. G. Henderson, M. H. Denton, P. C. Brandt, and J. Goldstein (2006), Analyzing electric field morphology through data-model comparisons of the Geospace Environment Modeling Inner Magnetosphere/Storm Assessment Challenge events, J. Geophys. Res., 111, A11S11, doi:10.1029/2006JA011700.
[13] Bame, S. J., et al. (1993), Magnetospheric plasma analyzer for spacecraft with constrained resources, Rev. Sci. Instrum., 64, 1026, doi:10.1063/1.1144173.
[14] Belian, R. D., G. R. Gisler, T. Cayton, and R. Christensen (1992), High-Z energetic particles at geosynchronous orbit during the great solar proton event series of October 1989, J. Geophys. Res., 97, 16,897, doi:10.1029/92JA01139.
[15] Liemohn, M. W., and M. Jazowski (2008), Ring current simulations of the 90 intense storms during solar cycle 23, J. Geophys. Res., 113, A00A17, doi:10.1029/2008JA013466.
[16] Shprits, Y. Y. , L. Chen, and R. M. Thorne (2009), Simulations of pitch angle scattering of relativistic electrons with MLT dependent diffusion coefficients, J. Geophys. Res., 114, A03219, doi:10.1029/2008JA013695.
[17] M. W. Liemohn, A. J. Ridley, N. Perlongo, J. Blears, and N. Yu. Ganushkina (Pending). Inner Magnetospheric keV-Energy Electrons and Their Influence on the Ionosphere-Thermosphere System. American Geophysical Union.